ACS APPLIED ENERGY MATERIALS
Cite This: ACS Appl. Energy Mater. 2019, 2, 4821−4832
Article
www.acsaem.org

Enhancing Efficiency and Stability of Hot Casting p−i−n Perovskite Solar Cell via Dipolar Ion Passivation

Kai-Chi Hsiao,[†,‡] Meng-Huan Jao,[†] Bo-Ting Li,[†] Ting-Han Lin,[§] Stan Hsueh-Chung Liao,[∥] Ming-Chung Wu,[§,⊥,#] and Wei-Fang Su*[,†,‡]

[†]Department of Materials Science and Engineering, National Taiwan University, Taipei City 10617, Taiwan
[‡]Department of Materials Science and Engineering, Advanced Research Center for Green Materials Science and Technology, National Taiwan University, Taipei City 10617, Taiwan
[§]Department of Chemical and Materials Engineering, Chang Gung University, Taoyuan City 33302, Taiwan
[∥]FrontMaterials Corporation Ltd., Taipei City 10087, Taiwan
[⊥]Green Technology Research Center, Chang Gung University, Taoyuan City 33302, Taiwan
[#]Division of Paediatrics Neonatology, Department of Paediatrics, Chang Gung Memorial Hospital, Taoyuan City 33305, Taiwan

Supporting Information

ABSTRACT: Anionic and cationic defects are considered as one of the crucial factors that affect carrier transport property and degradation of perovskite photovoltaic materials. Herein, we demonstrate a simple passivation of hot casted perovskite film in air by a dipolar ion, 2-thiophene ethylammonium chloride (TEACl), showing enhanced power conversion efficiency (PCE) of solar cell from 15.44% to 18.84% with increased open circuit voltage (V_{oc}) by 50 mV. The dipolar ion of TEACl can simultaneously passivate both cationic and anionic defects. Space charge limited current model, Urbach energy analysis, and photoluminescence spectroscopy were conducted and revealed that the defects passivated by TEACl reduced the defects density of perovskite films, nonradiative recombination, and electronic disorder. In addition, the device with TEACl passivation exhibited outstanding stability of power output (<0.1% decay) as compared with the device without passivation (>8% decay) from the 300 s measurement of current verse time plots ($J-T$ plots) at 65% relative humidity and 50 °C in air. The 80% of initial PCE was maintained after 700 h storage. As compared to conventional passivation approaches which are typically carried out at complicated crystallization step of perovskite, this post-treatment process can be easily done on the crystallized perovskite film. This facile approach is upscale and compatible with conventional coating techniques such as slot-die coating, spray, etc. for high-quality perovskite film.

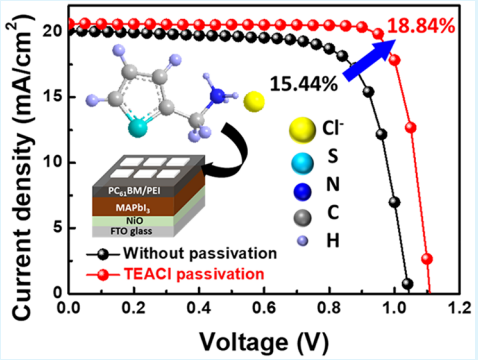

KEYWORDS: *perovskite, solar cell, hot casting, dipolar ion, solution process, passivation, stability*

1. INTRODUCTION

The organic−inorganic hybrid perovskite (OIHP) photovoltaic has drawn lots of attention since its first debut in 2009. The unique properties of OIHP such as high absorption coefficient in the visible light region,[1] relatively low exciton binding energy,[2−4] and long carrier lifetime[5] make it a potential candidate for the next generation photovoltaic technology. In the OIHP photovoltaic, there are two types of device architectures including conventional (n−i−p) and inverted (p−i−n) architectures. The n−i−p architecture means the device is assembled in the order of electron transport layer/perovskite active layer/hole transport layer,[6,7] whereas the p−i−n architecture is assembled in the reserved order.[8,9] For our work, we adapted the p−i−n architecture because of the ease of device fabrication, low temperature process (150 °C), and no hysteresis issue of device performance.

Nowadays, many research groups are improving the power conversion efficiency (PCE) of OIHP devices and anticipate bringing this technology into industry.[10] Over the past decade, the PCE of perovskite solar cell has been increased from 3.8% in 2009 [11] to 23.3% in 2018,[12] which is among the best performance obtained by thin film photovoltaics and is comparable to the well-developed Si solar cells. Up to now, for most high efficiency OIHP photovoltaics, the light absorbing active perovskite layer is deposited based on solvent engineering strategy, which creates a smooth and compact thin film by using antisolvent during the spin coating process. However, the complexity of solvent dripping procedure, the requirement of critical drip timing, and the excessive use of antisolvent limit the

Received: March 6, 2019
Accepted: June 25, 2019
Published: June 25, 2019

DOI: 10.1021/acsaem.9b00486
ACS Appl. Energy Mater. 2019, 2, 4821−4832

potential of upscale manufacture by this process. With the hot casting process, highly crystalline perovskite thin film can be formed within a few seconds by depositing precursor solution on heated substrate in air. The hot casted perovskite film exhibits high device performance.[13] The process is promising for scaling up from lab-scale small area to industry-scale large area module.[14]

The hot casting process can deliver large grain size and high crystalline perovskite thin film for high efficiency solar cell due to the fast evaporation of solvent on heated substrate.[13,15,16] Several research groups are dedicated to exploring the growth kinetics of perovskite thin film made by hot casting process and anticipate unveiling the relationship between crystallinity and device performance.[15,17] Nevertheless, the study of hot-casting-derived perovskite thin film mostly focused on increasing crystallinity or enlarging crystal size, while it is imperative to delicately passivate perovskite thin films to realize high efficiency and stable devices.

Despite the high crystallinity of silicon solar cell, the dangling bond at the surface of silicon is still regarded as a detrimental issue for deteriorating the device performance.[18,19] To annihilate dangling bond as well as increase PCE, surface passivation is a common approach in silicon solar cell, while in OIHP thin film, the uncoordinated lead (Pb^{2+}) and halide (X^-) induce positive and negative charge defects. Therefore, various molecules such as electron-donating Lewis base or electron-accepting Lewis acid were used to passivate the ionic defects in OIHP. The Lewis base molecules are good candidates, e.g., thiophene and pyridine, for surface passivation and trap state reduction of perovskite thin film due to their donor-like behaviors,[20−24] whereas the Lewis acid molecule, e.g., phenyl C61 butyric acid methyl ester ($PC_{61}BM$), acts as electron acceptor to passivate the uncoordinated halide induced deep trap state.[25] Additionally, the halide vacancies tend to degrade perovskite materials, in which the oxygen can be trapped in the halide vacancies to induce superoxide radical under illumination.[26] As a result, the photoinduced radicals degrade the perovskite into small volatile molecules.[27] Therefore, the passivation of the relevant defect-induced trap state in OIHP thin film is an effective method to improve PCE as well as the stability of OIHP solar cell.[28]

However, few of these molecules have the ability to simultaneously passivate both cationic and anionic defects in OIHP and most of these passivation approaches aim at OIHP thin film made from a complicate and difficult control antisolvent deposition during the crystallization step.[29−31] As a result, the corresponding passivation engineering with potential to large scale fabricated OIHP will be an issue.

Here in this work, we demonstrate a simple dipolar ion post treatment approach for hot casted perovskite film, which can simultaneously passivate cationic and anionic defects and improve the carrier mobility, thus enhancing the efficiency and stability of p−i−n planar solar cell. Among evaluated dipolar ions, 2-thiophene ethylammonium chloride (TEACl) shows enhanced power conversion efficiency (PCE) of solar cell from 15.44% to 18.84% and over 80% of initial PCE is maintained after 700 h storage. Spectroscopy, electronic, and device characterizations were systematically investigated to show the effective suppression of nonradiative recombination in perovskite film after the treatment of TEACl.

2. EXPERIMENTAL SECTION

Material Synthesis. For dipolar ions synthesis, 2-thiophene ethylammonium iodide, bromide, and chloride were synthesized by reacting with equal molar 2-thiophene ethylamine (Tokyo Chemical Industry Co., Ltd. 98%) and hydroiodic acid (Acros, 57% HI in ethanol), hydrobromic acid (Acros, 33% HBr in acetic acid), hydrochloric acid (Fisher, 36% in H_2O), respectively. Take TEAI for example, the equal molar 2-thiophene ethylamine and hydroiodic acid were first transferred into a three-neck flask. After vigorous stirring of the mixture for 2 h in an ice bath, the solvent was removed by a rotary evaporator to obtain a pale yellow powder. The powder was washed with diethyl ether (Fisher, 99%) until the color turned white. The white powder was further purified by recrystallization using anhydrous ethanol (Sigma-Aldrich, 99.5%). Subsequently, the white disk-like powder was dried in a vacuum oven at 70 °C overnight and stored in nitrogen filled glovebox.

Device Fabrication. The deposition protocol of p−i−n hot casting perovskite device was followed by the previous work in literature.[13] The fluorine-doped tin oxide (FTO)-coated glass substrates (Pilkington, 7 Ω/sq) were cleaned in the order of DI water, base solution, methanol, and isopropanol in ultrasonic bath for 15 min. Prior to the deposition of the hole transport layer, the UV−ozone treatment was carried out to again clean the FTO substrate. The hydrophilic substrate surface helps to obtain uniform nickel oxide, acting as hole transport layer. The $MAPbI_3$ perovskite solution was prepared by dissolving lead iodide (Alfa Aesar, 99.9985%) and methylammonium iodide (FrontMaterials Co. Ltd.) in equal stoichiometric mole in a cosolvent system of dimethyl sulfoxide (Acros, 99.7%) and γ-butyrolactone (Acros, 99+%) in 3:7 volume ratio. The mixture was stirred for 12 h at 70 °C before using. For perovskite film deposition, the as-prepared substrates (FTO/NiO) and precursor solution were preheated at 150 and 70 °C on the hot plate, respectively, for 10 min to reach thermal equilibrium. Around 50 μL of perovskite precursor solution was quickly dropped onto the hot substrate followed by spin coating at 4000 rpm for 15 s. The transparent yellow perovskite precursor became a black solid film in the beginning of the spin coating procedure that indicated the precursor turn to crystallized perovskite film immediately. For passivating the perovskite film, the passivation molecules, which were TEACl, TEABr, and TEAI, at 1−20 mM in isopropanol were preheated at 70 °C and then spin-coated on the top of crystallized perovskite film at 3000 rpm for 20 s. Prior to capping electron transport layer, here it was $PC_{61}BM$, the baking step (70 °C for 15 min) was carried out to remove residual solvent (IPA). Subsequently, 20 mg/mL $PC_{61}BM$ (FrontMaterials Co. Ltd. 99%) in chlorobenzene was spin-coated on passivated perovskite film at 1000 rpm for 30 s, whereas for the devices without passivation, the $PC_{61}BM$ was directly deposited on the crystallized perovskite film. Then, the work function modifier polyethylenimine (PEI) of 0.1 wt % dissolved in isopropanol was eventually spin-coated onto the electron transport layer at 4000 rpm for 30 s. The device was completed by the thermal evaporation of 100 nm silver electrode with an active area of 0.09 cm^2. For the results of device performance, they were summarized from the measurements of 24 devices made from 4 different batches. The electron-only and hole-only devices for space charge limited current (SCLC) model fitting were fabricated with the structure of FTO/compacted TiO_2/perovskite with or without passivation/$PC_{61}BM$/PEI/Au and FTO/NiO/perovskite with or without passivation/Au, respectively.

Characterization of Materials and Devices. The curves of photocurrent density (J)−voltage (V) of solar cell devices were measured in air under A.M. 1.5 irradiation (100 mW/cm^2) of a solar simulator source (YAMASHITA DENSO, YSS-200A, class AAA) equipped with a 1600 W xenon short arc lamp and a Keithley 2400 source meter. For each run of the test, the light intensity was calibrated with a monocrystalline silicon standard cell having KG-5 filter to adjust mismatched spectra to unity. The $J-V$ curves of devices with 0.09 cm^2 active area were obtained from both forward (from −0.2 to 1.2 V) and backward (from 1.2 to −0.2 V) scans. The step voltage of the test was fixed at 40 mV, and the delay time was fixed at 10 ms. Absorption spectra of the films were measured using a UV−vis spectrometer

DOI: 10.1021/acsaem.9b00486
ACS Appl. Energy Mater. 2019, 2, 4821−4832

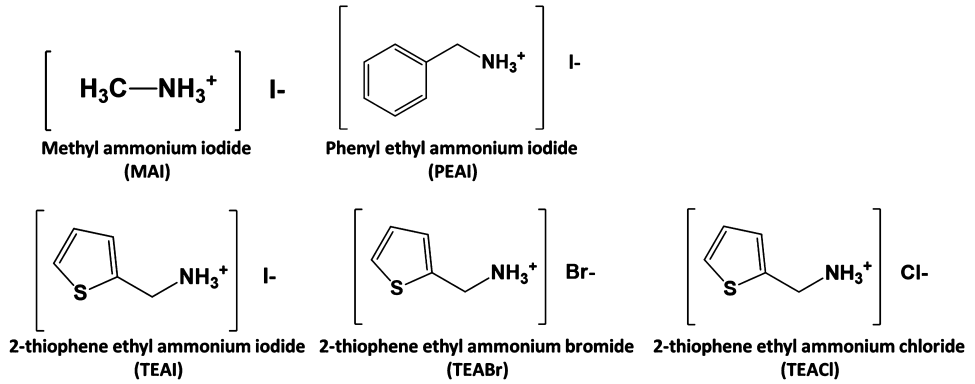

Figure 1. Chemical structures of passivation molecules.

Table 1. Photovoltaic Performance of Perovskite Solar Cells with/without Passivation Molecules

sample	V_{oc} (V)	J_{sc} (mA/cm^2)	FF (%)	PCE (%)
W/O passivation	1.05 ± 0.01	19.39 ± 0.48	73.26 ± 1.19	14.08 ± 0.26
W/IPA	0.92 ± 0.03	16.4 ± 0.86	50.88 ± 4.02	7.69 ± 0.41
W/MAI	0.94 ± 0.03	16.54 ± 0.67	56.40 ± 2.70	8.76 ± 0.79
W/PEAI	1.09 ± 0.00	18.08 ± 0.50	73.59 ± 1.68	14.50 ± 0.31
W/TEAI	1.09 ± 0.01	19.20 ± 0.38	74.03 ± 1.15	15.49 ± 0.38

(Hitachi, U-4100). To observe Urbach tail of perovskite films, the sensitive measurement using an integrating sphere to circumvent the light scattering from thin films was employed. The Urbach tail energy (E_u) calculation was followed with $\alpha = \alpha_0 \exp(h\nu/E_u)$. As we take the logarithm of this equation, the equation becomes $\ln(\alpha) = \ln(\alpha_0) + (h\nu/E_u)$. The term of $(h\nu/E_u)$ can be obtained from the slope of the straight line of plotting $\ln(\alpha)$ against the incident photon energy ($h\nu$). Finally, the Urbach energy (E_u) can be obtained from the reciprocal of the fitting slope, which is detailed in the main text of this paper. Steady-state photoluminescence (PL), continuous PL, and time-resolved PL (TRPL) were performed by exciting samples with a 440 nm continuous-wave diode laser (DONGWOO, PDLH-440-25). The transient TRPL was recorded by a time-correlated single photon counting (TCSPC) (WELLS-001 FX, DONGWOO OPTRON) spectrometer at a 312.5 MHz frequency with 2 ms duration. Electrochemical impedance spectroscopy (EIS) measurement was done by using impedance measurement unit (ZAHNER, elektrik PP210) under 1 sun illumination (100 mW/cm^2) with the same solar simulator as described before. The applied direct current (dc) voltage was fixed at 1.05 V for devices with FTO/NiO/perovskite with or without passivation/$PC_{61}BM$/PEI/Au with a 10 mV perturbation alternating current (ac). The frequency ranging from 10 kHz to 0.1 Hz was used. Cross-sectional FE-SEM samples were prepared from the actual device by mechanical glass cutter. The SEM images of devices were acquired by a field emission scanning electron microscope (Hitachi, SU8000, voltage 10 kV, working distance 8.0 mm). X-ray diffraction (XRD) patterns were obtained using high power (18 kW) X-ray diffractometer (Rigaku TTRAX 3) under Cu Kα radiation (λ = 1.5406 Å). The grazing-incidence wide-angle X-ray scattering (GIWAXS) spectra of samples were obtained using synchrotron X-ray spectroscopy (λ= 1.239 810 Å) at BL23A1 SWAXS end station of the National Synchrotron Radiation Research Center (NSRRC) in Hsinchu, Taiwan. The trap density and carrier mobility were calculated followed by space charge limited current (SCLC) model. For electron-only device, the architecture was FTO/TiO_2/$MAPbI_3$ with and without passivation/$PC_{61}BM$/PEI/Au, whereas for hole-only device, the architecture was FTO/NiO/perovskite with and without passivation/Au. The $I-V$ curve for the SCLC model fitting was measured in the dark from 0 to 3 V for electron-only device and from 0 to 5 V for hole-only device with a scan rate of 10 ms. The surface potential mapping of perovskite films with or without passivation was examined by Kelvin probe atomic force microscopy (KPFM, Dimension-3100 Multimode, Digital Instruments) with a Pt/Ir-coated tip in tapping mode. For surface potential difference, the samples were mapped in the dark or under λ = 550 nm LED light source (WLS-LED, Mightex) illumination at an angle of around 45°.

3. RESULTS AND DISCUSSION

The properties of perovskite can be manipulated with different stoichiometry of ammonium salt and lead halide because of the different contribution of p orbital of lead from lead iodide and of p orbital of halide from ammonium salt. The slight over ratio of ammonium salt or lead halide can facilitate the carrier transportation and improve the imbalance of carrier transfer rate due to a slight band shift of perovskite, which is closed to p-type or n-type property.[32] To maintain the ambipolar properties of perovskite thin films, the hot casting starts with stoichiometric amount of methylammonium iodide and lead iodide. Briefly, for hot casting perovskite films, the as-prepared substrates (FTO/NiO) and precursor solution (methylammonium lead triiodide, $CH_3NH_3PbI_3$) were preheated at 150 and 70 °C on the hot plate, respectively. Around 50 μL of perovskite precursor solution was quickly dropped onto the hot substrate followed by spin coating at 4000 rpm for 15 s. The crystallized perovskite films was formed immediately (details in the Experimental Section). The organoammonium iodide dipolar ion will be a good candidate to passivate both cation and anion defects present in perovskite film. Three organoammonium iodide dipolar ions were selected as passivation molecules: methylammonium iodide (MAI), phenylethylammonium iodide (PEAI), and 2-thiophene ethylammonium iodide (TEAI). Their chemical structures are shown in Figure 1. In order to dissolve the dipolar ions such as MAI, PEAI, and TEAI, one should use polar solvent such as methanol (MeOH), ethanol (EtOH), or isopropyl alcohol (IPA). However, the content of active hydrogen is high for MeOH (3.12 atom %) and EtOH (2.17 atom %) as compared with IPA (1.67 atom %). The active hydrogen of MeOH and EtOH quickly reacted with crystallized perovskite to form volatile methylamine (MA), hydroiodic acid (HI), and lead iodide (PbI_2)[33] as shown in Figure S1a. Thus, the IPA was used as the solvent to dissolve dipolar ions. Various concentrations of IPA solutions (1−20 mM) of dipolar ions

DOI: 10.1021/acsaem.9b00486
ACS Appl. Energy Mater. 2019, 2, 4821−4832

Table 2. Photovoltaic Performance of Solar Cells with and without TEA Series Passivation

sample	V_{oc} (V)	J_{sc} (mA/cm^2)	FF (%)	PCE (%)	Champ.PCE (%)
W/O passivation	1.05 ± 0.01	19.42 ± 0.56	71.70 ± 2.27	14.62 ± 0.45	15.44
W/TEACl	1.11 ± 0.00	20.47 ± 0.67	78.30 ± 2.11	17.78 ± 0.46	18.84
W/TEABr	1.10 ± 0.01	19.60 ± 0.78	76.46 ± 2.69	16.48 ± 0.75	17.32
W/TEAI	1.09 ± 0.01	19.43 ± 0.77	76.86 ± 1.55	16.27 ± 0.42	17.09

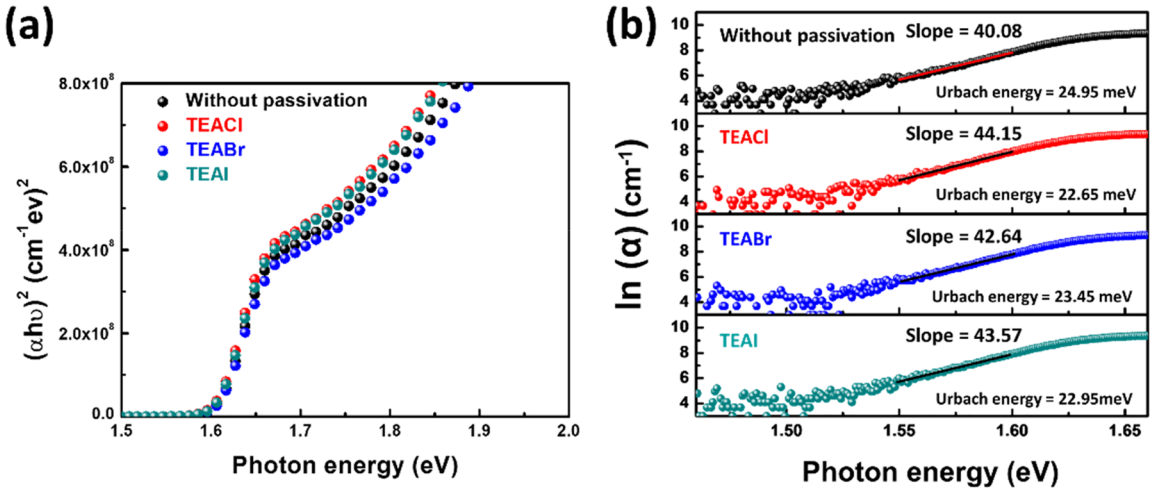

Figure 2. Characterization of perovskite films: (a) optical bandgap and (b) Urbach energy with/without passivation.

were prepared and used to treat the hot-casted perovskite thin films. The optimal concentraion of dipolar ions in IPA is determined to be 2.5 mM. Despiste minor changes observed in the film treated with IPA, it is still a good solvent for dipolar ions. Therefore, we used the film treated with pristine IPA as a control to figure out its effect on the device performance. Table 1 summaries the device performance with and without dipolar ion passivation. Although the perovskite film did not change much in appearance after the IPA or MAI/IPA treatment, the PCE of the device was reduced greatly from 14.08% to 7.69% and 8.76%, respectively. The passivation effect is observed for PEAI/IPA and TEAI/IPA treatment, and the PCE is increased to 14.50% and 15.49%, respectively.

To take a close look at the changes of perovskite films after each treatment, X-ray diffraction analyses were performed. It is interesting to note that the presence of dipolar ions in the IPA greatly retarded the activity of active hydrogen IPA owing to the salt effect. The peak of PbI_2 at around 12.5° can be clearly recognized from XRD pattern of perovskite films when they were treated with either IPA or MAI/IPA. On the other hand, the characteristic peak of PbI_2 cannot be observed from the films treated with either PEAI/IPA or TEAI/IPA as shown in Figure S1b of Supporting Information. The results indicate that the volatile and small size of MAI is not an effective passivation agent, and the compound decomposed into MA, HI, and PbI_2 during the postannealing of the treated film at 70 °C for 15 min. However, the extent of decomposition was less than that of pure IPA treatment.[34−37] The presence of PbI_2 in decomposed perovskite disturbed ambipolar properties of perovskite thin film, thus decreasing the device performance. While the perovskite films with PEAI and TEAI passivation showed similar appearance as the pristine perovskite film. For target devices, both PEAI and TEAI can passivate perovskite film and improve device performance. We speculate that both molecules contain aromatic structure, which is larger than methyl group of MAI, can stabilize the cation, and is less mobile than MAI. Thus, they can stay in place to passivate the defects to have high device performance. Moreover, the TEAI exhibited better device performance than PEAI because TEAI contains unshared electron of thio atom that can passivate better than PEAI.[20] The results can also be explained from their pK_a of dipolar ions (MAI = 10.64, PEAI = 9.83, and TEAI = 9.74). The small pK_a of TEAI provides more dissociated cations so that it can passivate the defects more efficiently.

Both anion (I^-) and cation (Pb^+) defects in perovskite need to be passivated. Thus, the choice of the anion in the passivation molecule is of equal importance as that of the cation. We fixed cation using TEA, then explored the role of different anions (their chemical structures are shown in Figure 1). The results are summarized in Table 2. The concentration of each passivation molecules was optimized (see Table S1 in Supporting Information). The device reaches the highest PCE of 18.84% by using chloride anion as compared to the other halide passivation molecules. The Cl^- is the smallest anion and exhibits the strongest electron affinity. In addition, the Pb−Cl bond has been reported to show stronger bonding than the Pb−I bond.[38] Therefore, as compared with other anions, the Cl^- anion can easily diffuse into perovskite and effectively bond with Pb ion. It implies that using passivation molecules containing Cl^- can facilitate not only the fast dissociation of organoammonium halide, e.g., TEACl, but also ease of diffusion into the perovskite film to compensate the positively charged anion defect (I^- vacancy).

In order to further investigate the effects of dipolar ion TEA halide in the post-treatment, characterizations using crystallography and spectroscopy were carried out. Figure S2a shows the $\theta-2\theta$ X-ray diffraction pattern of perovskite films with and without passivation. The diffraction peak at 13.8° and 19.7° can be indexed to be (110) and (200) of tetragonal phase $MAPbI_3$. The absence of PbI_2 peak at 12.7° indicates the perovskite precursor transferred to perovskite crystal completely using hot-casting process. To further gain insight into the changes of

DOI: 10.1021/acsaem.9b00486
ACS Appl. Energy Mater. 2019, 2, 4821−4832

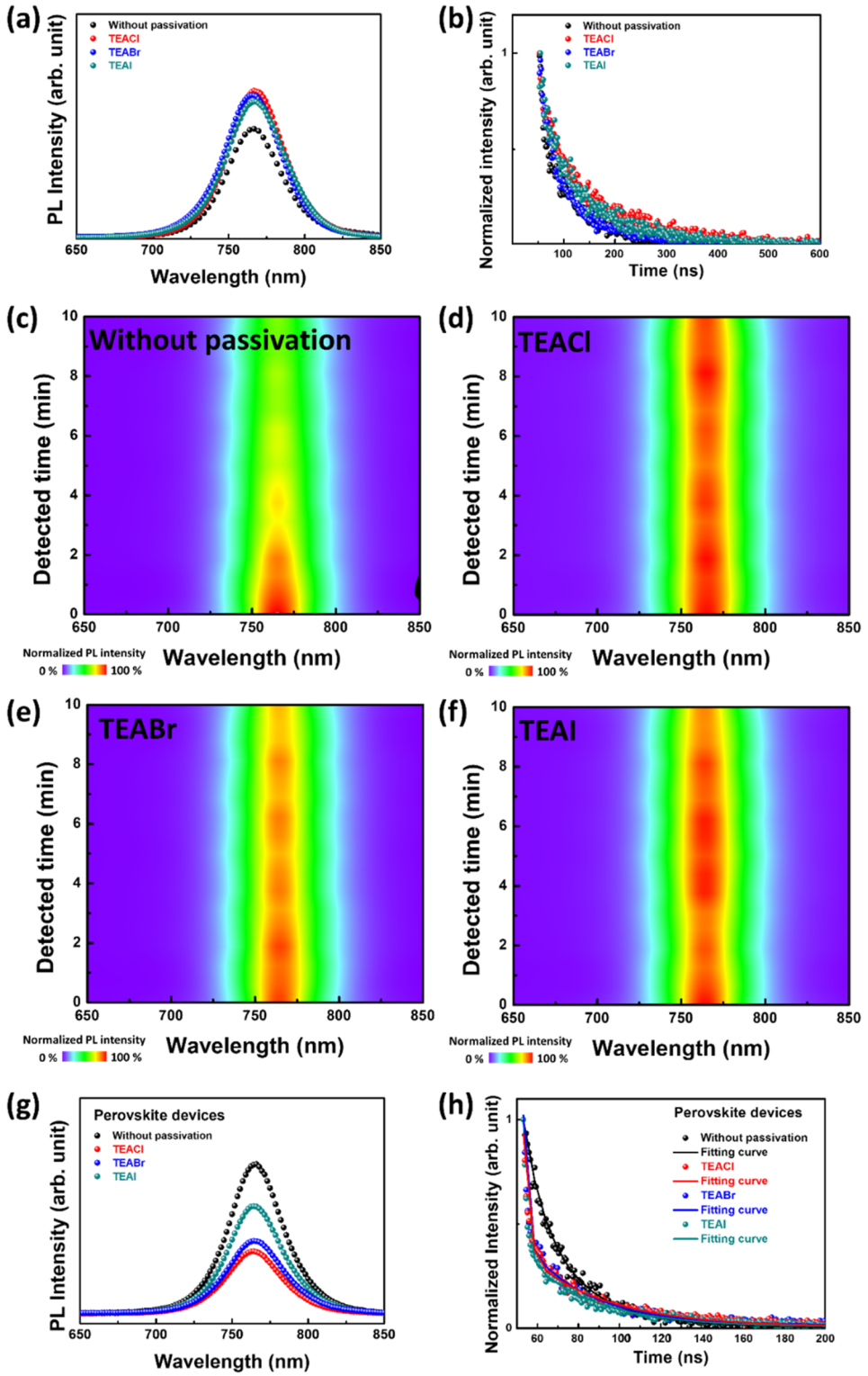

Figure 3. Effects of dipolar ions passivation on the photoluminescence profiles of perovskite film: (a) photoluminescence (PL) spectra, (b) time-resolved photoluminescence (TR-PL) profiles, continuous PL spectra of perovskite films (c) without and (d) with TEACl, (e) with TEABr, and (f) with TEAI passivation ((a)−(f) are the characteristics of perovskite films), and (g) PL spectra and (h) TR-PL profiles of perovskite films containing electron and hole transport layer.

crystallization behavior, grazing-incidence wide-angle X-ray scattering (GIWAXS) was conducted. Figure S2b is the integrated 1D patterns of perovskite films from the GIWAXS measurement. For overall integration of the GIWAXS pattern, only two characteristic peaks at Q = 10.2 nm^{-1} and 14.5 nm^{-1}, which can be referred as (110) and (200), were identified in Q range between 6−16 nm^{-1}. The absence diffraction signal in Q range lower than 10 nm^{-1} implies that the TEA halides do play passivation role instead of the formation of low dimensional structured perovskite.

DOI: 10.1021/acsaem.9b00486
ACS Appl. Energy Mater. 2019, 2, 4821−4832

From Table 2, we observe the enhanced device PCE by using TEA halide passivation, which is mainly resulted from the improvement of V_{oc}. Usually, the improvement of V_{oc} is from the enlargement of bandgap from the addition of ions into lattice structure or the formation of low dimensional structure of perovskite.[39−41] However, the XRD (Figure S2) and UV−vis (Figure 2) spectral analyses reveal negligible enlargement of the bandgap. Therefore, we deduce that the increased V_{oc} originated from the improved quality of perovskite thin film by treating it with TEA halide. To evaluate the inherent electronic properties of perovskite film with and without passivation, Urbach energy (E_μ) was employed to estimate the energetic disorder of the films. The Urbach equation is given in the following:

$$\alpha = \alpha_0 \exp\left(\frac{E}{E_u}\right)$$

Here, α represents the absorption coefficient of perovskite, E is the photon energy, and E_u is the Urbach energy. The calculated E_u of perovskite film without and with TEACl, TEABr, TEAI passivation from Figure 2b are 24.95, 22.65, 23.45, and 22.95 meV, respectively. The TEACl has the lowest E_u of 22.65 meV that indicates the least amount of defect states is present in the bandgap.

To probe the photogenerated carrier dynamics in the perovskite films, photoluminescence (PL) measurements were performed in air at room temperature. The PL spectra, continuous PL spectra, and time-resolved PL (TRPL) spectra of the films with and without passivation are shown in Figure 3. The films with passivation exhibit stronger steady-state PL intensity than perovskite without passivation as depicted in Figure 3a. The predominant photogenerated carriers in the perovskite are free electrons and holes because of the weak exciton binding energy.[42] The recombination rate of free carriers can be obtained from the TRPL spectra of perovskite films as shown in Figure 3b. The average lifetime (τ_{avg}) of charge carriers can be calculated according to the following equation, and the results are summarized in Table 3.

$$\tau_{avg} = \frac{A_1\tau_1 + A_2\tau_2}{A_1 + A_2}$$

Table 3. Calculated Average Carrier Lifetime of Perovskite Films with/without Passivation from Time-Resolved PL Measurements

sample	carrier lifetime (ns)
without passivation	53.46
W/TEACl	109.21
W/TEABr	76.87
W/TEAI	78.19

The carrier lifetime of perovskite films with passivation is longer than the film without passivation because of fewer defects and nonradiative recombination. The increased carrier lifetime confirms that the passivation can inhibit the presence of carrier scavengers from ionic defects. Among the passivation molecules, TEACl passivation exhibits the best and the longest average carrier lifetime of 109.21 ns.

The ionic defects, especially anion defects, of perovskite thin films provide a pathway for fast oxygen diffusion as the perovskite solar cell operated in ambient air.[43,26,44] With the presence of light, the oxygen molecules occupying halide vacancies act as electron scavengers. The electrons generated from perovskite directly react with oxygen and form superoxide radicals. The superoxide radicals adversely affect the stability of perovskite due to its strong oxidation ability. Figure 3c−f shows that the perovskite films with TEA halides passivation exhibited relatively stable PL intensity within 10 min of continuous measurement, whereas the PL intensity of perovskite film without passivation drops to around a 60% of initial PL intensity. The results indicate that the radiative recombination of photogenerated electrons is favored rather than reacted with oxygen and formed superoxide radicals in the passivated films. Thus, the rate of superoxide radicals formation slows down. Although the diffusion of oxygen into perovskite films is inevitable, decrease of the ionic defects, especially anion defects, is a key to reducing the formation of superoxide radicals and to enhancing the stability of perovskite devices operation in air.

We quantitatively estimated the charge transfer dynamics of perovskite device by TRPL measurement. All the TRPL profiles are well fitted by the biexponential decay model as shown in Figure 3h. The equation of the biexponential model is shown below. It depicts two decay mechanisms of charge carrier behaviors including fast decay and slow decay processes. For PL lifetime analysis, all of the devices were prepared in the architecture of FTO glass/NiO/perovskite without or with passivation/$PC_{61}BM$. Therefore, the fast decay of charge transfer process can be the result of the quenching of free carriers in the perovskite films through transport to hole transport layer (NiO) and electron transport layer ($PC_{61}BM$). On the other hand, the slow decay process can be the result of radiative decay.[45] As a result, the fast decay time (τ_1) and its proportion coefficient (A_1) represent the charge transfer of perovskite film. The other is slow decay time (τ_2) and its proportion coefficient (A_2), standing for the radiative recombination mechanism.[46,47]

$$I(t) = A_1 \exp\left(\frac{-t}{\tau_1}\right) + A_2 \exp\left(\frac{-t}{\tau_2}\right)$$

The proportions of two decay mechanisms of charge carrier behaviors and charge transfer time of each device can be evaluated by the fractions of their proportion coefficient. For instance, the fraction of $\frac{A_1}{(A_1 + A_2)}$ represents the ratio of charge transfer, whereas $\frac{A_2}{(A_1 + A_2)}$ is the ratio of radiative recombination in the entire decay process. The calculated results are summarized in Table 4. With the assistance of electron transport layer (ETL) of $PC_{61}BM$ and hole transport layer (HTL) of NiO, both perovskite films with or without passivation exhibit high proportion of charge transfer compared with the radiative recombination. The TRPL profiles of perovskite with TEACl show the steepest exponential profiles in the series and demonstrate the highest charge transfer proportion of decay

Table 4. Calculated Exciton Decay Time and % Proportion Coefficient of Charge Transfer from Biexponential Curves Fitting of Perovskite Devices with and without Passivation

sample	τ_1 (ns)	$A_1/(A_1 + A_2)$ (%)
W/O passivation	13.78	91.93
W/TEACl	3.15	99.99
W/TEABr	4.59	99.17
W/TEAI	6.73	95.95

DOI: 10.1021/acsaem.9b00486
ACS Appl. Energy Mater. 2019, 2, 4821−4832

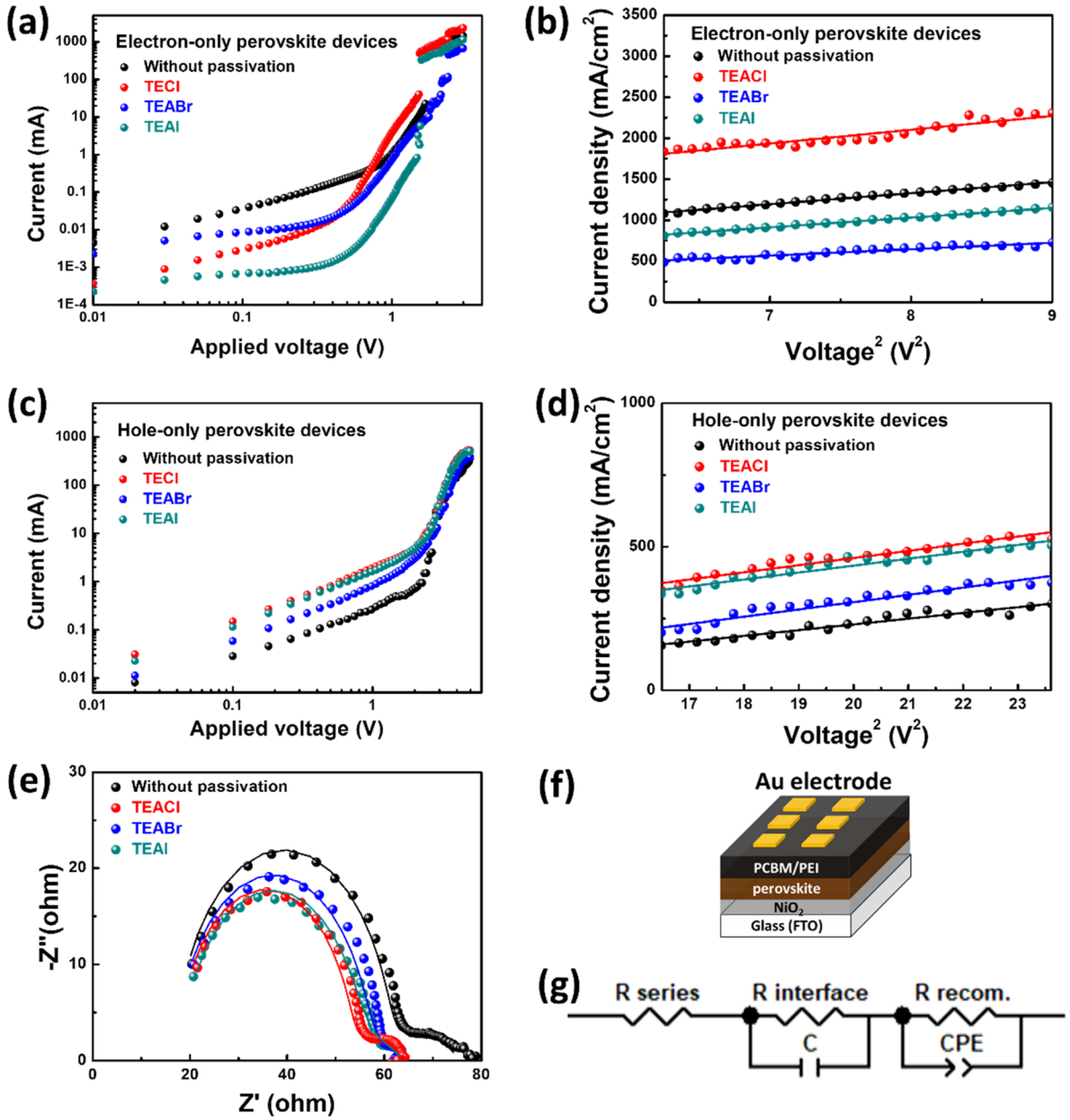

Figure 4. Space charge limit current model (SCLC) fitting of perovskite films without and with TEA halide passivation, electron-only devices: (a) $I-V$ curve and (b) $I-V^2$ at Child's region; hole-only devices (c) $I-V$ curve and (d) $I-V^2$ at Child's region; perovskite solar cells without and with TEA halide; (e) typical Nyquist plot; (f) device architecture; (g) equivalent circuit for model fitting.

mechanism with value more than 99%. The PL intensity in Figure 3g is consistent with the trend of charge transfer proportion. Moreover, the perovskite film with TEACl passivation exhibits the fastest charge transfer as compared with perovskite films without passivation or with other passivation molecules. The small anion of Cl^- with strong electron affinity and favorable band bending facilitates the electron transfer. Therefore, the presence of Cl^- at the interface between perovskite and $PC_{61}BM$, promotes the fastest charge transfer rate. The results confirm that through the passivation, the charge carrier can be transferred and extracted to respective electrodes efficiently once they are created.

To gain insights into mobility and trapped density in the perovskite films with and without passivation, measurements for space-charge limited current (SCLC) model were performed. Figure 4a and Figure 4c show the $I-V$ curves of the electron-only and hole-only devices of perovskite films, respectively. In the $I-V$ curve, it can be divided into three regions that are the ohmic region ($I \propto V$), trap-filled limit region (TFL region, $I \propto V^n$, $n > 2$), and Child's region ($I \propto V^2$). For the ohmic region and TFL region, the transition point between these two regions is known as trap filled limit voltage (V_{TFL}) according to the following equation:[48]

$$V_{TFL} = \frac{eN_t d^2}{2\varepsilon\varepsilon_0}$$

Here, e represents the elementary charge, ε and ε_0 are the dielectric constant of perovskite and the permittivity of free space, N_t is the trapped density of the thin film, and d is the thickness of perovskite films. The calculated N_t values from electron-only devices are 1.41×10^{16}, 3.33×10^{15}, 6.94×10^{15},

DOI: 10.1021/acsaem.9b00486
ACS Appl. Energy Mater. 2019, 2, 4821−4832

and 5.92×10^{15} (carrier number/cm^3), whereas for hole-only devices, the calculated N_t are 3.88×10^{16}, 1.70×10^{16}, 2.84×10^{16}, 2.85×10^{16} for perovskite films without passivation and with TEACl, TEABr, and TEAI passivation, respectively. It implies that fewer trapped states were present in the perovskite films with passivation than perovskite film without passivation for both electron-only and hole-only devices. The results prove that the TEA halides of dipolar ion passivation could compensate both types of ionic defects simultaneously and thus decrease the trap density of perovskite. In the Child's region (high applied voltage region), the carrier mobility (μ) can be derived from the following Mott−Gurney law:[49]

$$J = \frac{9\varepsilon\varepsilon_0\mu V^2}{8d^3}$$

The electron mobility (μ_e) can be obtained from Figure 4b, and the hole mobility (μ_h) can be obtained from Figure 4d. The results are summarized in Table 5 and show that the post-treatment of dipolar ion of TEA halides enhances electron and hole mobility from delicated passivation of ionic defects. The presence of Cl^- helps perovskite band bending (vide infra) and provides an efficient path for electron injection to electron transport layer.[50] Thus, for the passivation by TEACl, the Cl^- facilitates the electron extraction from perovskite to electron transport layer and exhibits the most significant enhancement of electron mobility.

Table 5. Calculated Carrier Mobility of Perovskite Devices without and with Passivation Using SCLC Modeling

sample	electron mobility (cm^2/(V·s))	hole mobility (cm^2/(V·s))
W/O passivation	1.96	0.40
W/TEACl	4.61	1.30
W/TEABr	3.44	1.12
W/TEAI	3.37	0.68

Besides the intrinsic properties of perovskite, the interface resistance between perovskite and electron transport layer also affects the performance of the device. The electrochemical impedance spectroscopy (EIS) of the device was carried out with applied bias near V_{oc} (1.05 V) under illumination to estimate the interface resistance ($R_{interface}$). Figure 4 shows the Nyquist plots of perovskite solar cell without and with passivation (e), devices structure (f), and equivalent circuit (g). The elements of the equivalent circuit include the series resistance of device (R_{series}), interfacial resistance ($R_{interface}$), and the recombination resistance of perovskite ($R_{recombination}$).[51] With the same hole transport layer and perovskite thickness, the $R_{interface}$ differences can be attributed to the passivation effects. From the model fitting of the equivalent circuit, the $R_{interface}$ between perovskite and electron transport layer can be calculated. The $R_{interface}$ of perovskite is around 45.6, 34.2, 34.5, 42.4 Ω for perovskite without passivation and with the passivation of TEACl, TEABr, and TEAI, respectively. Here, the TEACl passivation shows the lowest $R_{interface}$ of 34.2 Ω, which is in line with the result of high photovoltaic performance. For a brief summary, the devices with TEACl exhibit the best photovoltaic performance among devices (Supporting Information Figure S3). The anion effect of passivation molecules influences both transportation and mobility of charge carriers. The smallest size and strongest electron affinity of Cl^- among three TEA halides help to passivate the vacancy and extract electrons to electron transport layer effectively.

To understand the characteristics of charge recombination process between devices with and without TEACl passivation, the light dependent (from 1 to 100 mV/cm^2) photovoltaic performance was carried out and shown in Figure 5a and Figure 5b. According to the Langevin theory, the charge recombination mechanism can be depicted by the slope of the semilogarithmic plot of V_{oc} versus light intensity. The equation is expressed as the following:[52−54]

$$V_\lambda = V_s + \frac{nk_BT}{q}\ln\left(\frac{P_\lambda}{P_s}\right)$$

Here, the V_λ represents V_{oc} depending on light intensity; the V_s is V_{oc} under 100 mW/cm^2; the k_B is Boltzmann constant; T refers absolute temperature of 298 K; q is the elementary charge, and the P_λ and P_s are light intensity at different wavelength and standard sunlight intensity (100 mW/cm^2), respectively. The ideality factor (n) reveals the dominant type of recombination behaviors of devices, where ideality factor n = 1 indicates the bimolecular recombination and n = 2 represents the trap-assisted recombination.[54] In Figure 5b, compared with devices without passivation (n = 1.77), the trap-assisted recombination in devices can be significantly suppressed using TEACl passivation (n = 1.43) due to the reduced trap density in perovskite films.

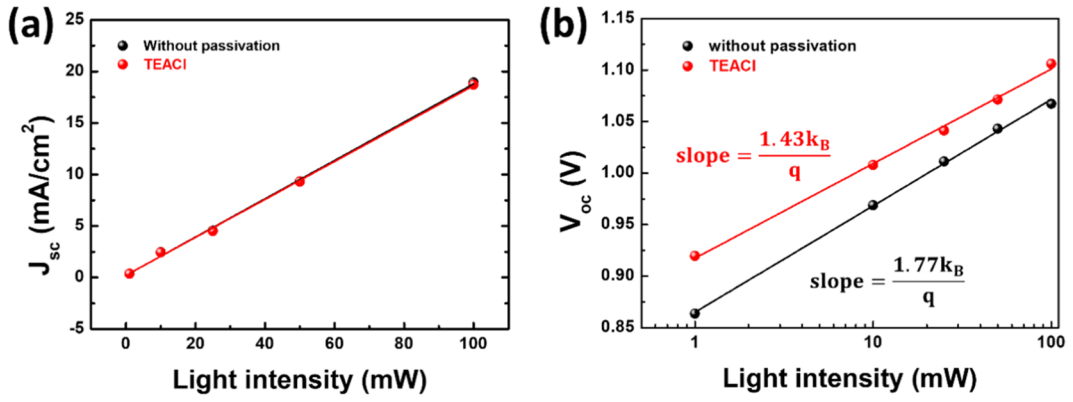

Figure 5. Dependent performance of devices without and with TEACl passivation on light intensity: (a) short-circuit current (J_{sc}) and (b) open-circuit voltage (V_{oc}).

DOI: 10.1021/acsaem.9b00486
ACS Appl. Energy Mater. 2019, 2, 4821−4832

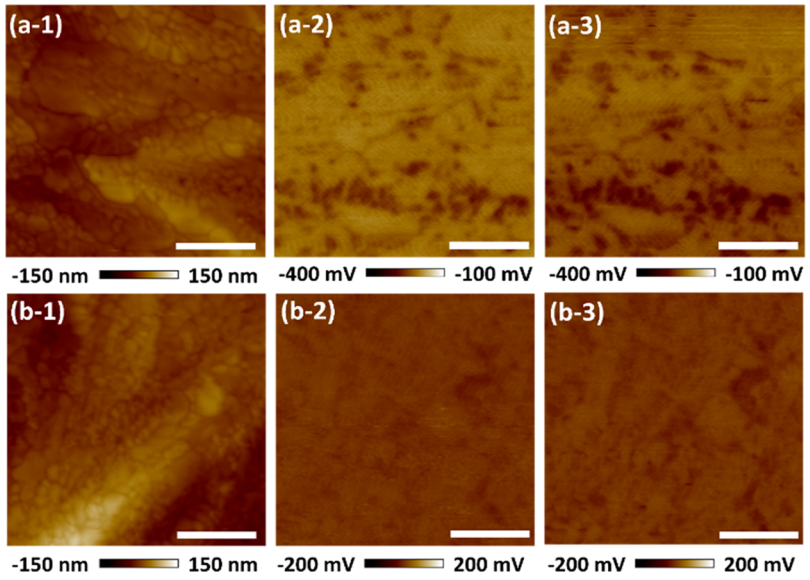

Figure 6. Surface characteristics of perovskite films without and with TEACl passivation: (a-1, b-1) topography mapping and (a-2, b-2) surface potential mapping in the dark; (a-3, b-3) under illumination (scale bar = 1 μm).

To observe the morphology of perovskite thin films and their charge transfer behaviors, the measurements of atomic force microscopy and Kelvin-probe atomic force microscopy were conducted. The topography is very similar for pristine perovskite film (Figure 6a-1), and theperovskite film with TEACl passivation (Figure 6 b-1). Both films were deposited on the hole transport layer. The grain sizes of both perovskite films are in hundred nanometer scale. The surface potential mapping of the perovskite with TEACl passivation in the dark are shown in Figure 6a-2 and Figure 6b-2 and under illuminationin Figure 6 a-3 and Figure 6b-3. The locations of surface potential mapping on the samples were fixed to observe the changes of surface potential from in dark to under illumination. The distribution of surface potential is very smooth for the film with passivation (−200 mV to 200 mV) as compared with the film without passivation (−400 mV to −100 mV). The change of surface potential is very minor from in dark to under illumination for the perovskite film with TEACl as compared with the film without it, which can be attributed to the slight band bending effect from the passivation. The dark spots with low surface potential indicate the grain boundaries and defects of the films as shown in Figure 6a-1 and Figure 6b-1. The grain boundaries and defects of the film trap carriers easily and therefore cause large change in surface potential under illumination. Apparently, the film without passivation contained many defects and boundaries and trapped carriers, whereas the TEACl passivation can reduce defects and suppress the carrier trapping.

Figure 7a shows the cross-sectional SEM images of perovskite devices. The configurations of devices fabricated from the perovskite film with and without TEACl passivation can be clearly observed. There are no differences in the layer structure and thickness for two devices. The thickness of each layer can be identified (NiO is around 100 nm; $CH_3NH_3PbI_3$ is 450 nm; $PC_{61}BM$ is 90 nm; Ag electron is 100 nm). The SEM images of other devices are shown in Figure S4. Figure 7b−e shows the photovoltaic distribution of 24 devices fabricated from the perovskite film with and without TEACl passivation. The results show high reproducibility of TEACl passivated devices. The average PCE of devices having TEACl passivation can be enhanced from 14.62% to 17.78%. Furthermore, the PCE of the champion device having TEACl passivation can be enhanced from the original 15.44% to 18.84% with no hysteresis as shown in Figure 7f. The outstanding PCE improvement is attributed to the increase of V_{oc} and fill factor. From the systematic analysis of perovskite with TEACl passivation, we demonstrate that ionic defects in perovskite film are successfully passivated and the nonradiative recombinations of charge carriers are reduced as well. The reduction of energy loss directly reflected by the enhancement of V_{oc} and PCE of the devices.

The maximum power point tracking of devices without encapsulation in ambient air directly indicate whether the photovoltaic performance of devices is stable in the presence of moisture and light. Generally, the presence of moisture, oxygen, and light is believed to gradually degrade the perovskite layer and therefore deteriorate the device performance. Reducing ionic defects in perovskite film can prevent it from the fast oxygen diffusion and thus improve the stability of devices. Figure 7g shows the 300 s maximum power point track (MPPT) of devices fabricated from perovskite film with and without TEACl passivation in air (relative humidity = 65%, operating temperature of devices = 50 °C). The devices were not encapsulated. Prior to the MPPT measurement of devices, the $J-V$ curves were measured to determine the optimal applied voltage of MPPT. The devices having TEACl passivation exhibit an extremely stable output with less than 0.1% PCE drop after 300 s measurement. The PCE can still maintain over 18.6% after 300 s measurement. However, the devices without passivation were vulnerable in air, and the irreversible PCE drop was larger than 8% from initial PCE of device. It clearly indicates that the deteriorated performance of device without passivation is more susceptible to heat and humidity than the device with TEACl passivation. For the intrinsic stability of perovskite, the device with and without passivation was stored in the same environment of nitrogen. As Figure 7h shows, the device without passivation can only maintain 80% of initial PCE in the first 400 h, whereas the device with TEACl passivation can maintain 80% of initial PCE over 700 h. It again provides evidence that the suppressed ionic defects in perovskite can prevent devices from defect assisted degradation.

DOI: 10.1021/acsaem.9b00486
ACS Appl. Energy Mater. 2019, 2, 4821−4832

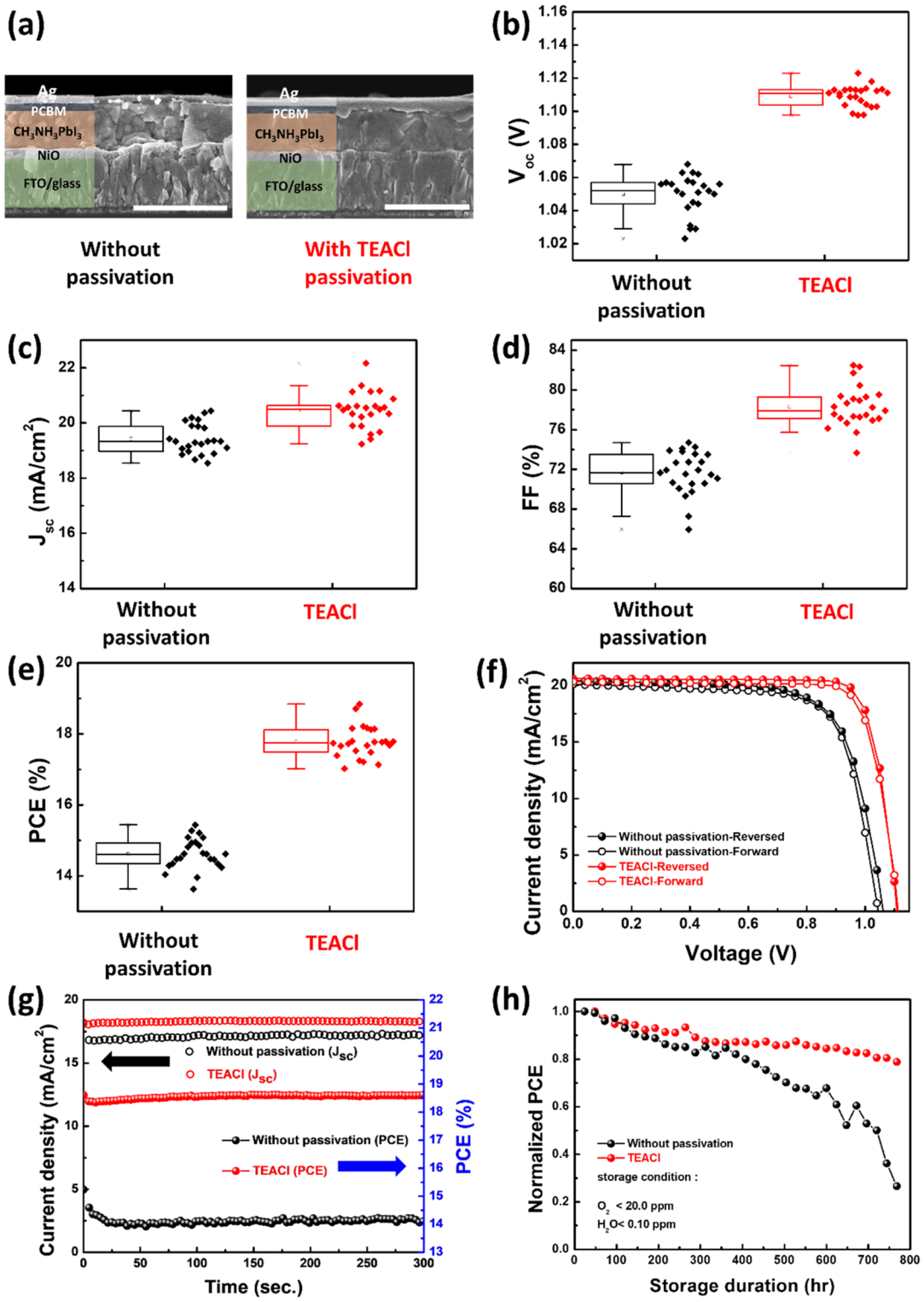

Figure 7. FE-SEM images of devices without and with TEACl passivation: (a) architecture and cross section (scale bar = 1 μm). Performance distribution of 24 devices: (b) V_{oc}, (c) J_{sc}, (d) fill factor, and (e) PCE. Performance of champion devices: (f) J–V curves, (g) steady-state photocurrent output PCE measured at the maximum power point (applied bias = 0.92 and 0.84 V for device with TEACl and without passivation). (h) Stability test for device storage in glovebox.

4. CONCLUSIONS

We systematically explored the passivation of ionic defects of hot casted perovskite film using various dipolar ions of organo-ammonium halide: MAI, PEAI, TEA halides. The dipolar ions can passivate both cationic and anionic defects simultaneously. Spectroscopy, electronic, and device characterizations were performed to investigate the TEA halides passivation effect. With the significant decrease of ionic defect density in perovskite and successful interfacial modification, the nonradiative recombination can be efficiently reduced and thereby enhance the open-circuit voltage and fill factor of the devices. The TEACl

DOI: 10.1021/acsaem.9b00486
ACS Appl. Energy Mater. 2019, 2, 4821−4832

is the most effective one because of its high ionization constant and small anion, The power conversion efficiency of planar p−i−n devices with TEACl passivation shows improved PCE from 15.44% to 18.89% as compared to perovskite solar cell without passivation. The results of maximum power output tracking of devices also demonstrate outstanding stability of devices with TEACl passivation. This facile surface passivation strategy is promising for preparing high quality stable perovskite solar cells using conventional upscale coating technology that paves the way for commercialization.

■ ASSOCIATED CONTENT

Supporting Information

The Supporting Information is available free of charge on the ACS Publications website at DOI: 10.1021/acsaem.9b00486.

Photography of perovskite films treated with various solvent and diopar ions in IPA and their XRD patterns, grazing-incidence wide-angle X-ray scattering (GIWAXS) spectra, performance distribution of devices, cross-sectional image from FE-SEM, and table of device PCE (PDF)

■ AUTHOR INFORMATION

Corresponding Author

*E-mail: suwf@ntu.edu.tw. Phone: +886 2 33664078. Fax: +886 2 23634562.

ORCID

Ming-Chung Wu: 0000-0002-3584-3871

Wei-Fang Su: 0000-0002-3375-4664

Notes

The authors declare no competing financial interest.

■ ACKNOWLEDGMENTS

This work was financially supported by the "Advanced Research Center for Green Materials Science and Technology" from The Featured Area Research Center Program within the framework of the Higher Education Sprout Project by the Ministry of Education (Grant 107L9006) and the Ministry of Science and Technology in Taiwan (Grants MOST106-2218-E-002-021-MY2 and 107-3017-F-002-001). The authors also thank the partial financial support from Grant MOST106-2923-M-002-004-MY3.

■ REFERENCES

(1) De Wolf, S.; Holovsky, J.; Moon, S.-J.; Löper, P.; Niesen, B.; Ledinsky, M.; Haug, F.-J.; Yum, J.-H.; Ballif, C. Organometallic Halide Perovskites: Sharp Optical Absorption Edge and Its Relation to Photovoltaic Performance. *J. Phys. Chem. Lett.* **2014**, *5* (6), 1035−1039.

(2) Kim, H.-S.; Lee, C.-R.; Im, J.-H.; Lee, K.-B.; Moehl, T.; Marchioro, A.; Moon, S.-J.; Humphry-Baker, R.; Yum, J.-H.; Moser, J. E.; Grätzel, M.; Park, N.-G. Lead iodide perovskite sensitized all-solid-state submicron thin film mesoscopic solar cell with efficiency exceeding 9%. *Sci. Rep.* **2012**, *2*, 591−591.

(3) Huang, J.; Yuan, Y.; Shao, Y.; Yan, Y. Understanding the physical properties of hybrid perovskites for photovoltaic applications. *Nat. Rev. Mater.* **2017**, *2*, 17042.

(4) Steirer, K. X.; Schulz, P.; Teeter, G.; Stevanovic, V.; Yang, M.; Zhu, K.; Berry, J. J. Defect Tolerance in Methylammonium Lead Triiodide Perovskite. *ACS Energy Lett.* **2016**, *1* (2), 360−366.

(5) Stranks, S. D.; Eperon, G. E.; Grancini, G.; Menelaou, C.; Alcocer, M. J. P.; Leijtens, T.; Herz, L. M.; Petrozza, A.; Snaith, H. J. Electron-Hole Diffusion Lengths Exceeding 1 Micrometer in an Organometal Trihalide Perovskite Absorber. *Science* **2013**, *342* (6156), 341−344.

(6) Momblona, C.; Gil-Escrig, L.; Bandiello, E.; Hutter, E. M.; Sessolo, M.; Lederer, K.; Blochwitz-Nimoth, J.; Bolink, H. J. Efficient vacuum deposited p-i-n and n-i-p perovskite solar cells employing doped charge transport layers. *Energy Environ. Sci.* **2016**, *9* (11), 3456−3463.

(7) Ryu, S.; Seo, J.; Shin, S. S.; Kim, Y. C.; Jeon, N. J.; Noh, J. H.; Seok, S. I. Fabrication of metal-oxide-free CH3NH3PbI3 perovskite solar cells processed at low temperature. *J. Mater. Chem. A* **2015**, *3* (7), 3271−3275.

(8) Seo, J.; Park, S.; Chan Kim, Y.; Jeon, N. J.; Noh, J. H.; Yoon, S. C.; Seok, S. I. Benefits of very thin PCBM and LiF layers for solution-processed p−i−n perovskite solar cells. *Energy Environ. Sci.* **2014**, *7* (8), 2642−2646.

(9) You, J.; Meng, L.; Song, T.-B.; Guo, T.-F.; Yang, Y.; Chang, W.-H.; Hong, Z.; Chen, H.; Zhou, H.; Chen, Q.; Liu, Y.; De Marco, N.; Yang, Y. Improved air stability of perovskite solar cells via solution-processed metal oxide transport layers. *Nat. Nanotechnol.* **2016**, *11*, 75.

(10) Lamberti, F.; Litti, L.; De Bastiani, M.; Sorrentino, R.; Gandini, M.; Meneghetti, M.; Petrozza, A. High-Quality, Ligands-Free, Mixed-Halide Perovskite Nanocrystals Inks for Optoelectronic Applications. *Adv. Energy Mater.* **2017**, *7* (8), 1601703.

(11) Kojima, A.; Teshima, K.; Shirai, Y.; Miyasaka, T. Organometal Halide Perovskites as Visible-Light Sensitizers for Photovoltaic Cells. *J. Am. Chem. Soc.* **2009**, *131* (17), 6050−6051.

(12) https://www.nrel.gov/pv/assets/images/efficiency-chart.png.

(13) Liao, H.-C.; Guo, P.; Hsu, C.-P.; Lin, M.; Wang, B.; Zeng, L.; Huang, W.; Soe, C. M. M.; Su, W.-F.; Bedzyk, M. J.; Wasielewski, M. R.; Facchetti, A.; Chang, R. P. H.; Kanatzidis, M. G.; Marks, T. J. Enhanced Efficiency of Hot-Cast Large-Area Planar Perovskite Solar Cells/Modules Having Controlled Chloride Incorporation. *Adv. Energy Mater.* **2017**, *7* (8), 1601660.

(14) Galagan, Y.; Di Giacomo, F.; Gorter, H.; Kirchner, G.; de Vries, I.; Andriessen, R.; Groen, P. Roll-to-Roll Slot Die Coated Perovskite for Efficient Flexible Solar Cells. *Adv. Energy Mater.* **2018**, *8* (32), 1801935.

(15) Nie, W.; Tsai, H.; Asadpour, R.; Blancon, J.-C.; Neukirch, A. J.; Gupta, G.; Crochet, J. J.; Chhowalla, M.; Tretiak, S.; Alam, M. A.; Wang, H.-L.; Mohite, A. D. High-efficiency solution-processed perovskite solar cells with millimeter-scale grains. *Science* **2015**, *347* (6221), 522−525.

(16) Zheng, Y. C.; Yang, S.; Chen, X.; Chen, Y.; Hou, Y.; Yang, H. G. Thermal-Induced Volmer−Weber Growth Behavior for Planar Heterojunction Perovskites Solar Cells. *Chem. Mater.* **2015**, *27* (14), 5116−5121.

(17) Nie, W.; Tsai, H.; Blancon, J.-C.; Liu, F.; Stoumpos, C. C.; Traore, B.; Kepenekian, M.; Durand, O.; Katan, C.; Tretiak, S.; Crochet, J.; Ajayan, P. M.; Kanatzidis, M.; Even, J.; Mohite, A. D. Critical Role of Interface and Crystallinity on the Performance and Photostability of Perovskite Solar Cell on Nickel Oxide. *Adv. Mater.* **2018**, *30* (5), 1703879.

(18) Yan, B.; Yue, G.; Sivec, L.; Yang, J.; Guha, S.; Jiang, C.-S. Innovative dual function nc-SiOx:H layer leading to a > 16% efficient multi-junction thin-film silicon solar cell. *Appl. Phys. Lett.* **2011**, *99* (11), 113512.

(19) Glunz, S. W.; Feldmann, F. SiO2 surface passivation layers − a key technology for silicon solar cells. *Sol. Energy Mater. Sol. Cells* **2018**, *185*, 260−269.

(20) Noel, N. K.; Abate, A.; Stranks, S. D.; Parrott, E. S.; Burlakov, V. M.; Goriely, A.; Snaith, H. J. Enhanced Photoluminescence and Solar Cell Performance via Lewis Base Passivation of Organic−Inorganic Lead Halide Perovskites. *ACS Nano* **2014**, *8* (10), 9815−9821.

(21) Lee, J.-W.; Bae, S.-H.; Hsieh, Y.-T.; De Marco, N.; Wang, M.; Sun, P.; Yang, Y. A Bifunctional Lewis Base Additive for Microscopic Homogeneity in Perovskite Solar Cells. *Chem.* **2017**, *3* (2), 290−302.

(22) Juang, T.-Y.; Kao, J.-C.; Wang, J.-C.; Hsu, S.-Y.; Chen, C.-P. Carbonized Bamboo-Derived Carbon Nanodots as Efficient Cathode Interfacial Layers in High-Performance Organic Photovoltaics. *Adv. Mater. Interfaces* **2018**, *5* (10), 1800031.

(23) Guo, Y.; Ma, J.; Lei, H.; Yao, F.; Li, B.; Xiong, L.; Fang, G. Enhanced performance of perovskite solar cells via anti-solvent

DOI: 10.1021/acsaem.9b00486
ACS Appl. Energy Mater. 2019, 2, 4821−4832

nonfullerene Lewis base IT-4F induced trap-passivation. *J. Mater. Chem. A* **2018**, *6* (14), 5919−5925.
(24) Li, H.; Tao, L.; Huang, F.; Sun, Q.; Zhao, X.; Han, J.; Shen, Y.; Wang, M. Enhancing Efficiency of Perovskite Solar Cells via Surface Passivation with Graphene Oxide Interlayer. *ACS Appl. Mater. Interfaces* **2017**, *9* (44), 38967−38976.
(25) Niu, T.; Lu, J.; Munir, R.; Li, J.; Barrit, D.; Zhang, X.; Hu, H.; Yang, Z.; Amassian, A.; Zhao, K.; Liu, S. Stable High-Performance Perovskite Solar Cells via Grain Boundary Passivation. *Adv. Mater.* **2018**, *30* (16), 1706576.
(26) Aristidou, N.; Eames, C.; Sanchez-Molina, I.; Bu, X.; Kosco, J.; Islam, M. S.; Haque, S. A. Fast oxygen diffusion and iodide defects mediate oxygen-induced degradation of perovskite solar cells. *Nat. Commun.* **2017**, *8*, 15218.
(27) O'Mahony, F. T. F.; Lee, Y. H.; Jellett, C.; Dmitrov, S.; Bryant, D. T. J.; Durrant, J. R.; O'Regan, B. C.; Graetzel, M.; Nazeeruddin, M. K.; Haque, S. A. Improved environmental stability of organic lead trihalide perovskite-based photoactive-layers in the presence of mesoporous TiO2. *J. Mater. Chem. A* **2015**, *3* (14), 7219−7223.
(28) Zheng, X.; Chen, B.; Dai, J.; Fang, Y.; Bai, Y.; Lin, Y.; Wei, H.; Zeng, X. C.; Huang, J. Defect passivation in hybrid perovskite solar cells using quaternary ammonium halide anions and cations. *Nat. Energy* **2017**, *2*, 17102.
(29) Yang, M.; Zhang, T.; Schulz, P.; Li, Z.; Li, G.; Kim, D. H.; Guo, N.; Berry, J. J.; Zhu, K.; Zhao, Y. Facile fabrication of large-grain CH3NH3PbI3-xBrx films for high-efficiency solar cells via CH3NH3Br-selective Ostwald ripening. *Nat. Commun.* **2016**, *7*, 12305.
(30) Fu, F.; Pisoni, S.; Weiss, T. P.; Feurer, T.; Wäckerlin, A.; Fuchs, P.; Nishiwaki, S.; Zortea, L.; Tiwari, A. N.; Buecheler, S. Compositionally Graded Absorber for Efficient and Stable Near-Infrared-Transparent Perovskite Solar Cells. *Adv. Sci.* **2018**, *5* (3), 1700675.
(31) Kim, S.-G.; Chen, J.; Seo, J.-Y.; Kang, D.-H.; Park, N.-G. Rear-Surface Passivation by Melaminium Iodide Additive for Stable and Hysteresis-less Perovskite Solar Cells. *ACS Appl. Mater. Interfaces* **2018**, *10* (30), 25372−25383.
(32) Wang, Q.; Shao, Y.; Xie, H.; Lyu, L.; Liu, X.; Gao, Y.; Huang, J. Qualifying composition dependent p and n self-doping in CH3NH3PbI3. *Appl. Phys. Lett.* **2014**, *105* (16), 163508.
(33) Chang, C.-Y.; Huang, Y.-C.; Tsao, C.-S.; Su, W.-F. Formation Mechanism and Control of Perovskite Films from Solution to Crystalline Phase Studied by in Situ Synchrotron Scattering. *ACS Appl. Mater. Interfaces* **2016**, *8* (40), 26712−26721.
(34) Nagabhushana, G. P.; Shivaramaiah, R.; Navrotsky, A. Direct calorimetric verification of thermodynamic instability of lead halide hybrid perovskites. *Proc. Natl. Acad. Sci. U. S. A.* **2016**, *113* (28), 7717−7721.
(35) Juarez-Perez, E. J.; Ono, L. K.; Maeda, M.; Jiang, Y.; Hawash, Z.; Qi, Y. Photodecomposition and thermal decomposition in methylammonium halide lead perovskites and inferred design principles to increase photovoltaic device stability. *J. Mater. Chem. A* **2018**, *6* (20), 9604−9612.
(36) Fan, Z.; Xiao, H.; Wang, Y.; Zhao, Z.; Lin, Z.; Cheng, H.-C.; Lee, S.-J.; Wang, G.; Feng, Z.; Goddard, W. A.; Huang, Y.; Duan, X. Layer-by-Layer Degradation of Methylammonium Lead Tri-iodide Perovskite Microplates. *Joule* **2017**, *1* (3), 548−562.
(37) Dualeh, A.; Gao, P.; Seok, S. I.; Nazeeruddin, M. K.; Grätzel, M. Thermal Behavior of Methylammonium Lead-Trihalide Perovskite Photovoltaic Light Harvesters. *Chem. Mater.* **2014**, *26* (21), 6160−6164.
(38) Bond Energies. In *Encyclopedia of Inorganic Chemistry*; King, R. B., Ed.; Wiley, 2006.
(39) McMeekin, D. P.; Sadoughi, G.; Rehman, W.; Eperon, G. E.; Saliba, M.; Hörantner, M. T.; Haghighirad, A.; Sakai, N.; Korte, L.; Rech, B.; Johnston, M. B.; Herz, L. M.; Snaith, H. J. A mixed-cation lead mixed-halide perovskite absorber for tandem solar cells. *Science* **2016**, *351* (6269), 151−155.
(40) Cao, D. H.; Stoumpos, C. C.; Farha, O. K.; Hupp, J. T.; Kanatzidis, M. G. 2D Homologous Perovskites as Light-Absorbing Materials for Solar Cell Applications. *J. Am. Chem. Soc.* **2015**, *137* (24), 7843−7850.
(41) Quan, L. N.; Yuan, M.; Comin, R.; Voznyy, O.; Beauregard, E. M.; Hoogland, S.; Buin, A.; Kirmani, A. R.; Zhao, K.; Amassian, A.; Kim, D. H.; Sargent, E. H. Ligand-Stabilized Reduced-Dimensionality Perovskites. *J. Am. Chem. Soc.* **2016**, *138* (8), 2649−2655.
(42) Trinh, M. T.; Wu, X.; Niesner, D.; Zhu, X. Y. Many-body interactions in photo-excited lead iodide perovskite. *J. Mater. Chem. A* **2015**, *3* (17), 9285−9290.
(43) Bryant, D.; Aristidou, N.; Pont, S.; Sanchez-Molina, I.; Chotchunangatchaval, T.; Wheeler, S.; Durrant, J. R.; Haque, S. A. Light and oxygen induced degradation limits the operational stability of methylammonium lead triiodide perovskite solar cells. *Energy Environ. Sci.* **2016**, *9* (5), 1655−1660.
(44) Aristidou, N.; Sanchez-Molina, I.; Chotchuangchutchaval, T.; Brown, M.; Martinez, L.; Rath, T.; Haque, S. A. The Role of Oxygen in the Degradation of Methylammonium Lead Trihalide Perovskite Photoactive Layers. *Angew. Chem., Int. Ed.* **2015**, *54* (28), 8208−8212.
(45) Liang, P.-W.; Liao, C.-Y.; Chueh, C.-C.; Zuo, F.; Williams, S. T.; Xin, X.-K.; Lin, J.; Jen, A. K.-Y. Additive Enhanced Crystallization of Solution-Processed Perovskite for Highly Efficient Planar-Heterojunction Solar Cells. *Adv. Mater.* **2014**, *26* (22), 3748−3754.
(46) Chang, C.-Y.; Wang, C.-P.; Raja, R.; Wang, L.; Tsao, C.-S.; Su, W.-F. High-efficiency bulk heterojunction perovskite solar cell fabricated by one-step solution process using single solvent: synthesis and characterization of material and film formation mechanism. *J. Mater. Chem. A* **2018**, *6* (9), 4179−4188.
(47) Wu, M.-C.; Chan, S.-H.; Lee, K.-M.; Chen, S.-H.; Jao, M.-H.; Chen, Y.-F.; Su, W.-F. Enhancing the efficiency of perovskite solar cells using mesoscopic zinc-doped TiO2 as the electron extraction layer through band alignment. *J. Mater. Chem. A* **2018**, *6* (35), 16920−16931.
(48) Heo, J. H.; You, M. S.; Chang, M. H.; Yin, W.; Ahn, T. K.; Lee, S.-J.; Sung, S.-J.; Kim, D. H.; Im, S. H. Hysteresis-less mesoscopic CH3NH3PbI3 perovskite hybrid solar cells by introduction of Li-treated TiO2 electrode. *Nano Energy* **2015**, *15*, 530−539.
(49) Chiang, C.-H.; Wu, C.-G. Bulk heterojunction perovskite−PCBM solar cells with high fill factor. *Nat. Photonics* **2016**, *10*, 196.
(50) Colella, S.; Mosconi, E.; Pellegrino, G.; Alberti, A.; Guerra, V. L. P.; Masi, S.; Listorti, A.; Rizzo, A.; Condorelli, G. G.; De Angelis, F.; Gigli, G. Elusive Presence of Chloride in Mixed Halide Perovskite Solar Cells. *J. Phys. Chem. Lett.* **2014**, *5* (20), 3532−3538.
(51) Yang, L.; Cai, F.; Yan, Y.; Li, J.; Liu, D.; Pearson, A. J.; Wang, T. Conjugated Small Molecule for Efficient Hole Transport in High-Performance p-i-n Type Perovskite Solar Cells. *Adv. Funct. Mater.* **2017**, *27* (31), 1702613.
(52) Xie, F.; Chen, C.-C.; Wu, Y.; Li, X.; Cai, M.; Liu, X.; Yang, X.; Han, L. Vertical recrystallization for highly efficient and stable formamidinium-based inverted-structure perovskite solar cells. *Energy Environ. Sci.* **2017**, *10* (9), 1942−1949.
(53) Tress, W.; Yavari, M.; Domanski, K.; Yadav, P.; Niesen, B.; Correa Baena, J. P.; Hagfeldt, A.; Graetzel, M. Interpretation and evolution of open-circuit voltage, recombination, ideality factor and subgap defect states during reversible light-soaking and irreversible degradation of perovskite solar cells. *Energy Environ. Sci.* **2018**, *11* (1), 151−165.
(54) Sherkar, T. S.; Momblona, C.; Gil-Escrig, L.; Ávila, J.; Sessolo, M.; Bolink, H. J.; Koster, L. J. A. Recombination in Perovskite Solar Cells: Significance of Grain Boundaries, Interface Traps, and Defect Ions. *ACS Energy Lett.* **2017**, *2* (5), 1214−1222.

DOI: 10.1021/acsaem.9b00486
ACS Appl. Energy Mater. 2019, 2, 4821−4832